Zirconium Carbide Clusters Stabilized within Carbon Cages

Yi Shen,[1†] Laura Abella,[2†] Yang-Rong Yao,[1*] Qingyu Meng,[1] Rongrong Luo,[1] Bei Li,[1] Zixin Wu,[1] Josep M. Poblet,[2] Antonio Rodríguez-Fortea,[2*] and Ning Chen[1*]

[1] College of Chemistry, Chemical Engineering and Materials Science, and State Key Laboratory of Radiation Medicine and Protection, Soochow University, Suzhou, Jiangsu 215123, P. R. China

[2] Departament de Química Física i Inorgànica. Universitat Rovira i Virgili, Marcel·lí Domingo 1, 43007 Tarragona, Spain

KEYWORDS: Cluster, Fullerene, Zirconium, DFT

ABSTRACT: Zirconium-based endohedral metallofullerenes (EMFs) were first detected in the gas phase in 1992, but their bulk synthesis has remained elusive over the past three decades. Herein, we present the first successful synthesis of Zr-based EMFs, addressing this longstanding challenge in fullerene chemistry. By utilizing an optimized synthesis strategy with zirconium carbide as the metal source, we obtained three Zr-based carbide clusterfullerenes, namely $Zr_2C_2@D_{3h}(5)$-C_{78}, $Zr_2C_2@I_h(7)$-C_{80}, and $Zr_3C_2@I_h(7)$-C_{80}. Single-crystal X-ray diffraction analyses revealed that the Zr_2C_2 clusters adopt a planar rhombic configuration bridged by a $(C\equiv C)^{2-}$ unit, while the Zr_3C_2 cluster exhibits a rare trifoliate geometry with a bridging $(C\text{-}C)^{6-}$ unit. The coordination modes in these Zr-based clusters are different from those observed in conventional organozirconium complexes, highlighting the unique coordination environments within fullerene cages. Combined experimental and theoretical studies further reveal the electronic structures of the Zr-based EMFs as $(Zr_2C_2)^{6+}@(C_{2n})^{6-}$ ($2n$ = 78, 80) and $(Zr_3C_2)^{6+}@(I_h(7)\text{-}C_{80})^{6-}$. This breakthrough in the synthesis of Zr-based EMFs not only offers new insights into the mechanisms of arc-discharge reaction and the formation of EMFs but also provides a substantial guideline for the encapsulation of new elements into fullerene cages, establishing a foundation for the design and synthesis of novel EMFs.

INTRODUCTION

Endohedral metallofullerenes (EMFs) are a unique kind of core-shell nanocarbon that metal atoms or clusters are encapsulated within the interior of carbon cages.[1-2] By judicious selection of the encapsulated metals, EMFs can be endowed with tailored physicochemical properties, making them highly promising for applications in biomedicine, single-molecule magnets, single-molecule devices, and quantum information storage.[3-7] For example, the high-spin ground state of gadolinium (Gd)-based EMFs has been employed to serve as molecular high-spin qubits, while the incorporation of dysprosium (Dy) or terbium (Tb) yields stable high-performance single-molecule magnets.[8-9] More recently, neodymium (Nd)-encapsulated EMF has been shown to facilitate charge extraction in perovskite solar cells, significantly boosting their efficiency and stability.[10] All these achievements are directly related to the properties of encapsulated metals and the versatile structures of the encapsulated moieties.

However, in contrast to the extensive studies on lanthanide-based EMFs, investigations of transition-metal encapsulation remain scarce, even though the d-orbital electrons of transition metals often afford richer redox chemistry and more versatile electronic structures than the f-orbital electrons of lanthanide metals.[11-13] For instance, titanium (Ti) can adopt both Ti(III) and Ti(IV) oxidation states inside carbon cages, enabling significant changes in electronic configuration and cluster geometry.[14] Moreover, exploring the encapsulation of transition metals is critical not only for fullerene chemistry but also for advancing novel transition metal materials, such as MXenes (e.g., Ti_3C_2 and Zr_3C_2) and metallo-carbohedrenes (e.g., Ti_8C_{12} and $Ti_{12}C_{12}$).[15-19] Encapsulating these transition-metal carbide species into fullerene cages could offer an atomically precise platform for understanding the bonding nature of these systems, tailoring their structural design and property exploration.

To date, successful encapsulation of transition metals in fullerenes has been limited to titanium, vanadium, and, very recently, nickel.[12, 20-23] Other transition metals have been explored only through theoretical studies or detected via mass spectrometry, with no scalable synthetic routes reported.[24-25] Among these, zirconium (Zr) is considered one of the most promising candidates being encapsulated because, as early as 1992, Smalley and colleagues detected the mass signal of $Zr@C_{28}$ using laser ablation techniques, demonstrating the feasibility of encapsulation of Zr.[26] Nevertheless, despite the continuous synthetic efforts in the past three decades, no breakthroughs have been achieved in the bulk synthesis of Zr-based EMFs, leaving it a longstanding challenge in fullerene chemistry.[27-28] Thus, it is highly desirable to develop synthetic methods to encapsulate new kinds of metals into the fullerene cages, which may lead to a breakthrough in their applications.[29]

Herein, we report the successful synthesis of Zr-based EMFs for the first time, tackling the three-decade challenge. An optimized synthesis strategy was developed to obtain three Zr-based carbide clusterfullerenes (CCF), namely $Zr_2C_2@D_{3h}(5)$-C_{78}, $Zr_2C_2@I_h(7)$-C_{80}, and $Zr_3C_2@I_h(7)$-C_{80}. The three Zr-based EMFs were successfully characterized by single-crystal X-ray diffraction (SC-XRD), matrix-assisted laser desorption ionization time-of-flight mass spectrometry (MALDI-TOF-MS), ultraviolet-visible-near infrared (UV-vis-NIR) absorption spectroscopy, together with density functional theory (DFT)

calculations. This work not only offers structural understanding into three novel Zr-based carbide clusterfullerenes but also provides new insights into the mechanisms of arc-discharge reaction and the formation of EMFs. Furthermore, this work also provides a substantial guideline for the encapsulation of new elements into fullerene cages, establishing a foundation for the design and synthesis of novel EMFs.

RESULTS AND DISCUSSION

Exploration of Synthetic Pathways for Zr-Containing EMFs. EMFs are typically synthesized using the Krätschmer-Huffman direct-current (DC) arc-discharge method. To synthesize the Zr-containing EMFs, we initially employed Zr_2O_3 as the zirconium source. A mixture of Zr_2O_3 and graphite powder was packed into a drilled graphite rod at a Zr:C molar ratio of 1:15, serving as the anode, while a graphite plate was used as the cathode. The packed graphite rods were initially subjected to high-temperature pre-treatment at 1000 °C for 20 hours,[30] followed by being installed in an arcing reactor. The arc-discharge reaction was performed under 200 Torr of He atmosphere with a current of 100 A, yielding black soot as the product. However, mass spectrometric analysis of the soot revealed the presence of only empty fullerenes, with no detectable signals corresponding to Zr-containing EMFs (Figure S1).

Next, we explored the trimetallic nitride template (TNT) method, which takes advantage of the propensity of rare-earth metals, such as Sc, to form trimetallic nitride clusters. This method facilitates the incorporation of certain metals into mixed trimetallic nitride clusters, as exemplified by the successful synthesis of $Sc_xV_{3-x}N@C_{2n}$.[23] In this study, Sc_2O_3 and ZrO_2 were employed as the metal sources (molar ratio of Sc:Zr:C = 1:1:15), and the reaction was conducted under 200 Torr of He and an additional 4 Torr of N_2. However, no signals corresponding to mixed nitride clusterfullerenes $Sc_xZr_{3-x}N@C_{2n}$ or any other Zr-containing EMFs could be detected by mass spectrometry (Figure S1), indicating that the TNT method was unsuccessful in synthesizing Zr-containing EMFs.

Unexpectedly, replacing ZrO_2 with ZrC as the zirconium source led to the unambiguous detection of Zr-containing EMFs in the mass spectra. The usage of ZrC as the metal source was reported in early studies, but molecular charaterization of the products is still absent.[31] Figure 1 compares the chromatograms obtained under identical separation conditions for the three synthetic pathways, along with the corresponding mass spectra. Neither the Zr_2O_3-based pathway nor the TNT method produced any detectable mass signals for Zr-containing EMFs. In contrast, the ZrC-based pathway yielded distinct mass signals for Zr_2C_{80}, with isotopic distributions in perfect agreement with theoretical predictions. Moreover, additional signals corresponding to other Zr-containing EMFs, such as Zr_2C_{82} and Zr_3C_{82}, were also observed exclusively in the ZrC-based pathway (Figure S1), confirming the successful synthesis of Zr-containing EMFs via the ZrC-based pathway and thus tackling the three-decade challenge. Finally, approximately 0.2 mg of Zr_2C_{80} and Zr_2C_{82}, and 0.1 mg of Zr_3C_{82} were obtained from 300 carbon rods.

Role of ZrC in Zr-EMF Synthesis. These results are particularly striking, as arc-discharge reactions have long been considered an atomization-driven process.[32] For example, abundant monometallic EMFs have been successfully synthesized using metal oxides as precursors, indicating that these oxides are decomposed into metal atoms, which are subsequently encapsulated into fullerene cages.[33-36] From this perspective, changing the initial metal precursors should not significantly alter the final products, as all precursors are expected to decompose into metal atoms. This approach using metal oxides as precursors has been proven effective for synthesizing most f-block EMFs but has not been successful for transition metals beyond Ti and V. In addition, metal sulfides were also employed in the early studies. For example, Popov and co-workers reported the successful synthesis of sulfide clusterfullerenes using Dy_2S_3 as the precursor.[37] However, our results demonstrate that modifying the precursor material enables the synthesis of previously inaccessible Zr-containing EMFs, which reforms the conventional understanding of a complete atomization process for arc-discharge reactions and suggests the involvement of a more complicated reaction pathway.

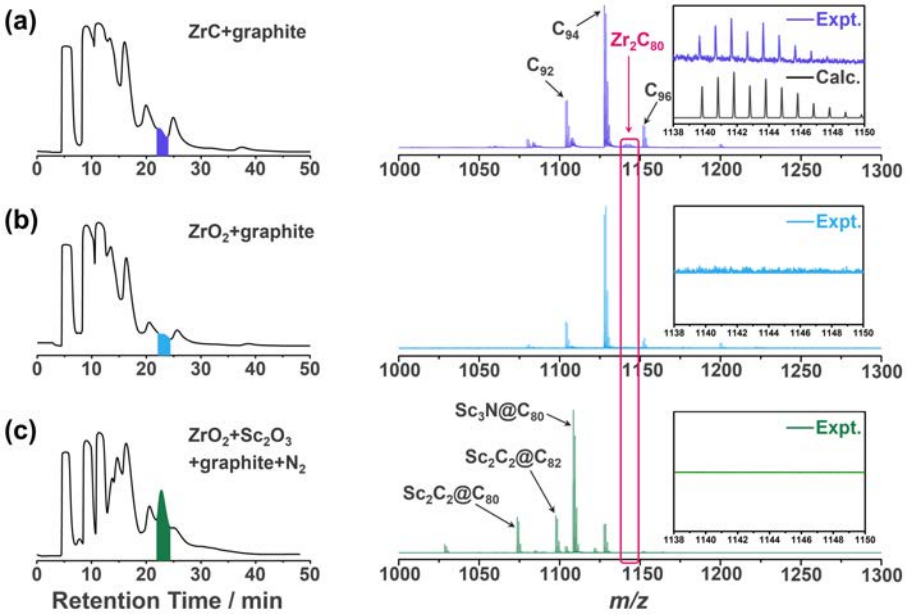


Figure 1. (Left) The HPLC profiles for the extracted fullerene solution using different synthetic methods: **(a)** ZrC, **(b)** ZrO_2, **(c)** ZrO_2 and Sc_2O_3 as the metal sources. The color-highlighted segments in the HPLC profiles are the fractions containing Zr_2C_{80}. (Right) The corresponding MALDI-TOF mass spectra of the highlighted fractions from 22 to 24 min. The mass peak of Zr_2C_{80} is encircled in red. The insets show the experimental mass signals and the theoretical isotopic distribution for Zr_2C_{80} magnified for more precise observation.

A plausible explanation for the successful synthesis of Zr-containing EMFs using ZrC is that ZrC is fragmented into small Zr_xC_y clusters under arc-discharge conditions. These Zr_xC_y clusters are highly reactive due to the presence of carbon atoms with dangling bonds, which readily interact with vaporized carbon species from graphite to facilitate the formation of complete fullerene cages. Based on the results, we propose that Zr atoms have limited reactivity with ambient carbon species, which explains why using ZrO_2 as the precursor fails to produce Zr-containing EMFs. Although ZrO_2 is expected to decompose into Zr atoms under arc-discharge conditions, it does not promote the formation of highly reactive Zr_xC_y fragments. In contrast, using ZrC as the precursor directly fosters the formation of these reactive Zr_xC_y fragments, which are essential for the formation of Zr-containing EMFs. Notably, other metals, such as Ti, lanthanides, and actinides, are able to react with carbon species to form M_xC_y fragments, leading to the formation of various mono-metallic, di-metallic, or carbon-clustered EMFs.

Importantly, this hypothesis extends to a broader discussion regarding the formation mechanism of EMFs. Currently, two prevailing models describe the formation mechanism of EMFs: the top-down and the bottom-up mechanisms.[38-42] Among these, the bottom-up mechanism can explain how a closed fullerene cage grows, but cannot fully reveal how the initial precursors form into EMFs in the arc-discharge environment. Our results can provide significant insights into this unresolved question and suggest that the initial precursors likely proceed through a fragment recombination or growth process, in which the metal-carbon clusters serve as templates that guide cage closure and metal encapsulation. This perspective extends the bottom-up mechanism, providing a more comprehensive framework for understanding EMF formation from raw materials. Nevertheless, the formation of EMFs remains a highly complex process, requiring extensive investigations for a more complete mechanistic understanding in the future.

Isolation of Zr_2C_{80}, Zr_2C_{82}, and Zr_3C_{82}. The Zr-containing EMFs were extracted from the synthesized soot using CS_2 as the extraction solvent. Afterward, the raw solution was evaporated to remove CS_2 completely and subsequently redissolved in toluene for purification. A multistage high-performance liquid chromatography (HPLC) procedure was employed to isolate the Zr-containing EMFs. Three target compounds, Zr_2C_{80}, Zr_2C_{82}, and Zr_3C_{82}, were successfully isolated through this process, as presented in Figures S2-4. Figure 2 shows the MALDI-TOF mass spectra of the three purified compounds under positive-ion mode, revealing only a single set of peaks centered at 1139.556, 1163.530, and 1253.489 *m*/*z*, corresponding to Zr_2C_{80}, Zr_2C_{82}, and Zr_3C_{82}, respectively. Additionally, the experimental isotopic distributions for all three Zr-containing EMFs were in excellent agreement with their calculated predictions.

Structural Analysis of Zr_2C_{80} and Zr_2C_{82}. The molecular structures of the purified Zr_2C_{80}, Zr_2C_{82}, and Zr_3C_{82} were characterized using SC-XRD analysis. Ni^{II}(OEP) (OEP = 2, 3, 7, 8, 12, 13, 17, 18-octaethylporphin dianion) was used as a cocrystallization agent to obtain high-quality crystals. The introduction of Ni^{II}(OEP) not only facilitates crystal growth but also restricts the rotational motion of the fullerene cages, thereby enhancing crystallization quality. The detailed crystallographic parameters for the resulting cocrystals are summarized in Table S1. In all three cocrystals, the shortest Ni-cage distances were measured in a narrow range of 2.763(9)-2.787(11) Å, indicating a substantial π-π interaction between the Ni^{II}(OEP) molecules and the fullerene cages.

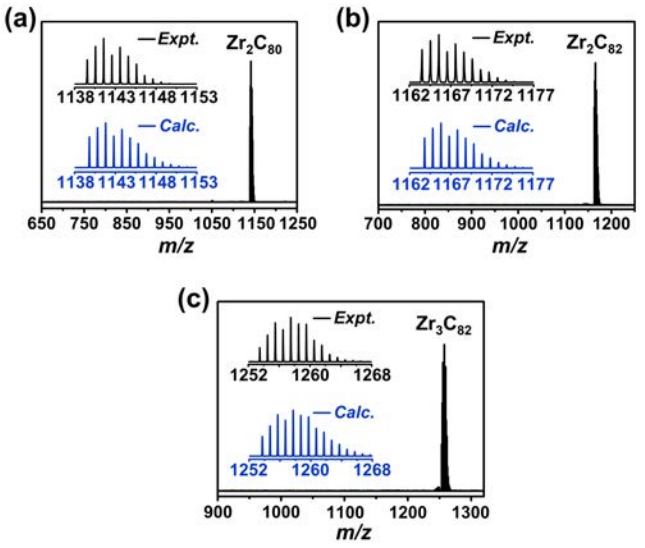


Figure 2. MALDI-TOF mass spectra of purified **(a)** Zr_2C_{80}, **(b)** Zr_2C_{82}, and **(c)** Zr_3C_{82} under positive-ion mode. The insets show the experimental and theoretical isotopic distribution for the three compounds.

The crystallographic structures of Zr_2C_{80} and Zr_2C_{82} were identified as $Zr_2C_2@D_{3h}(5)$-C_{78} and $Zr_2C_2@I_h(7)$-C_{80}, respectively, revealing that both are carbide clusterfullerenes rather than di-metallofullerenes, as illustrated in Figures 3a-b. These crystallographic results unambiguously confirm that the transition metal Zr has been experimentally encapsulated in the fullerene cages.

The space groups of $Zr_2C_2@D_{3h}(5)$-C_{78} and $Zr_2C_2@I_h(7)$-C_{80} are $P2_1/c$ (No. 14) and $C2/m$ (No. 12), respectively, both of which are commonly observed in EMF-Ni^{II}(OEP) cocrystallization systems. Both $Zr_2C_2@D_{3h}(5)$-C_{78} and $Zr_2C_2@I_h(7)$-C_{80} exhibit two distinct orientations of their carbon cages. For $Zr_2C_2@D_{3h}(5)$-C_{78}, the two orientations are related by a 60° rotation around the C_3 axis, coupled with a slight displacement. The occupancies of these orientations are 0.53 and 0.47, respectively, which can be considered approximately equal within the margin of refinement error. In contrast, $Zr_2C_2@I_h(7)$-C_{80} displays two orientations related by perfect mirror symmetry along the crystallographic mirror plane, with equal occupancies of 0.5.

The encapsulated Zr_2C_2 clusters display some disorder. For $Zr_2C_2@D_{3h}(5)$-C_{78}, six configurations of the Zr_2C_2 cluster within two cage orientations are observed, but the major one can be easily distinguished since it has the highest occupancy, which is much higher than the rest of the minor ones. For $Zr_2C_2@I_h(7)$-C_{80}, three configurations of the Zr_2C_2 cluster within one cage orientation are observed, and similarly, the major configuration has a much higher occupancy than the other two. The disorder information of the cluster of these two cocrystals is listed in Tables S2-3. For clarity, only one cage

orientation accompanied by the major Zr_2C_2 cluster configuration is discussed.

Self-adaptation of the Zr_2C_2 Clusters. The encapsulated Zr_2C_2 cluster adopts a rhombic configuration in both cages, with the Zr-C_2-Zr dihedral angles of 178.2° in C_{78} and 175.8° in C_{80}, respectively (Figures 3c-d). In $Zr_2C_2@D_{3h}(5)$-C_{78}, the two Zr atoms are positioned near the centers of hexagons along the C_3 axis, with Zr-cage distances ranging from 2.192(12) to 2.328(10) Å. In $Zr_2C_2@I_h(7)$-C_{80}, the Zr atoms are located beneath two opposite hexagons along a C_2 axis but slightly off-center, leading to a broader Zr-cage distance range of 2.088(14) to 2.420(12) Å. This deviation suggests that the Zr_2C_2 cluster undergoes subtle structural adaptation to accommodate the different fullerene cage environments. The Zr-Zr distances in C_{78} and C_{80} are 4.563(2) Å and 4.333(3) Å, respectively, indicating a more stretched Zr_2C_2 configuration in C_{78}. This elongation results in longer Zr-C distances (2.273(12)-2.410(12) Å) in C_{78} than those in C_{80} (2.210(16)-2.289(15) Å) and a shorter central C≡C bond length in C_{78} (1.135(18) Å) compared to that in C_{80} (1.212(15) Å), further demonstrating the structural adaptability of the Zr_2C_2 cluster in response to the spatial environments imposed by the fullerene cages.

Theoretical calculations were conducted to validate these structural configurations. The optimized geometries exhibit good agreement with experimental data (Figure S5), with detailed comparisons in Tables S4-5. Additional calculations of alternative Zr positions within the C_{78} cage showed that all tested configurations converged to the experimentally observed structure, except for one 26 kcal·mol^{-1} higher in energy (Figure S6). Similarly, in C_{80}, only one alternative configuration was found, which is 13 kcal·mol^{-1} higher in energy and features a butterfly-like geometry (Figure S7). These results strongly support the experimentally determined cluster orientations and highlight the energetic preference for the observed rhombic structures.

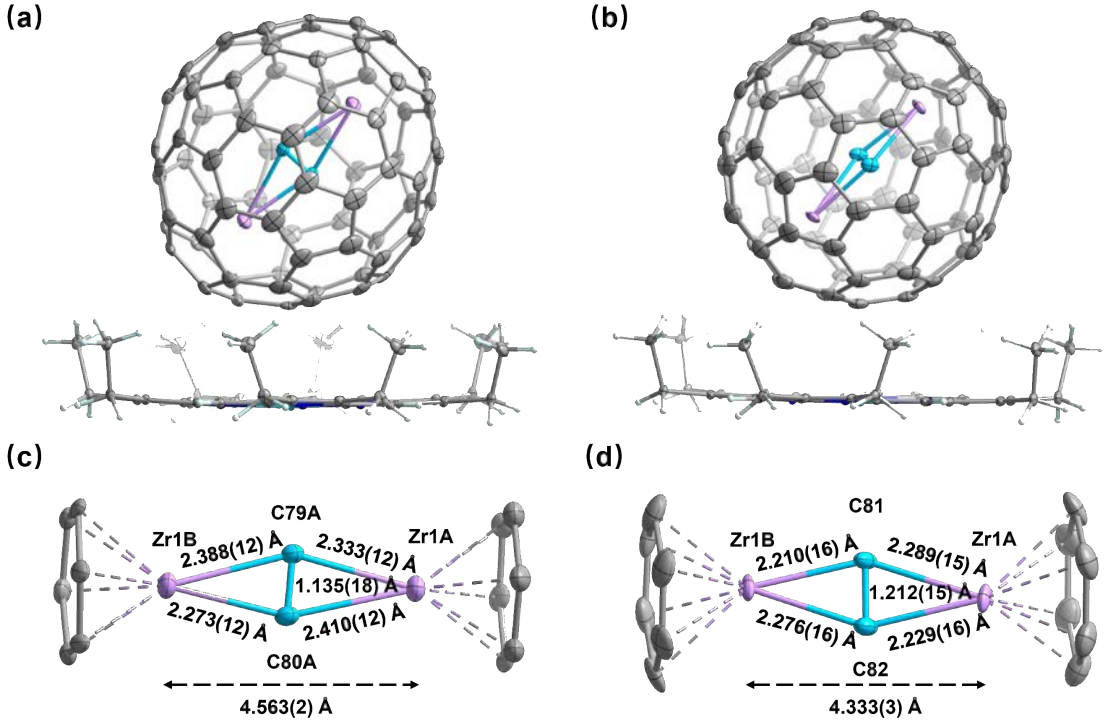


Figure 3. ORTEP drawing of **(a)** $Zr_2C_2@D_{3h}(5)$-C_{78}·[Ni^{II}OEP] and **(b)** $Zr_2C_2@I_h(7)$-C_{80}·[Ni^{II}OEP] with 20% thermal ellipsoids. Only the major cage and Zr_2C_2 orientations are shown, and the solvent molecules are omitted for clarity. **(c-d)** Fragment view of the relationship between the Zr_2C_2 cluster and the closest cage portion in **(c)** $D_{3h}(5)$-C_{78} and **(d)** $I_h(7)$-C_{80}. The cage C atoms are colored gray, and the encapsulated Zr and C atoms are highlighted as lavender and sky blue, respectively. Atomic distances are plotted in Å.

The rhombic configuration of Zr_2C_2 is similar to those of $Sc_2C_2@D_{2d}(23)$-C_{84} and $Dy_2C_2@D_2(35)$-C_{88},[43-44] but differs from previously reported M_2C_2 clusters, which predominantly adopt either a butterfly-like (e.g., $Sc_2C_2@C_{82}$,[43] $Ti_2C_2@C_{82}$,[14] $Gd_2C_2@C_{84}$,[45] $Tm_2C_2@C_{82}$,[46] and $U_2C_2@C_{78\text{-}80}$[47]) or a zigzag-like geometry (e.g., $Sc_2C_2@C_{88}$,[48] $Ti_2C_2@C_{78}$[14]). This variation in M_2C_2 configurations is influenced not only by the size and shape of the fullerene cage but also by the ionic radii of the metal centers. For instance, in $M_2C_2@D_{3h}(5)$-C_{78} (M = Ti, Zr, U), Ti_2C_2 adopts a zigzag configuration, whereas U_2C_2 assumes a butterfly-like structure. This divergence is attributed to the differences in the ionic radii of the metal centers: Ti^{4+} (0.61 Å) leads to a longer Ti-Ti separation, while U^{4+} (0.89 Å) results in a more compressed cluster. With an intermediate ionic radius of 0.72 Å, Zr^{4+} adopts a rhombic configuration, representing a structural transition between the zigzag and butterfly geometries. These findings highlight the structural adaptability of M_2C_2 clusters within fullerene cages and underscore the crucial role of metal ionic size in determining cluster geometry.

Structural Analysis of Zr_3C_{82}. The structure of Zr_3C_{82} was unambiguously determined as $Zr_3C_2@I_h(7)$-C_{80} using the Ni^{II}(OEP) co-crystallization method, as shown in Figure 4a. Notably, $Zr_3C_2@C_{80}$ represents the first instance of a transition metal M_3C_2 cluster encapsulated within a fullerene cage. Although Ti and Zr belong to the same group of transition metals, Ti-based carbide clusters have been observed in fullerene cages in the form of M_2C_2 and M_3C_3 clusters but lack the M_3C_2 cluster, which may result from the radius difference of Ti and Zr.

Like $Zr_2C_2@C_{80}$, the crystal structure of $Zr_3C_2@C_{80}$ belongs to the *C*2/*m* space group, indicating that the molecule exists in two orientations with equal occupancy, related by a crystallographic mirror plane. Within the Zr_3C_2 cluster, the central C_2 unit is fully ordered, and the primary Zr positions can be easily determined, as their occupancy is significantly higher than that of the minor disordered sites (Table S6). As illustrated in Figure 4b, all three Zr atoms are located near [5,6,6] junctions, similar to those observed in $M_3N@C_{80}$.[11]

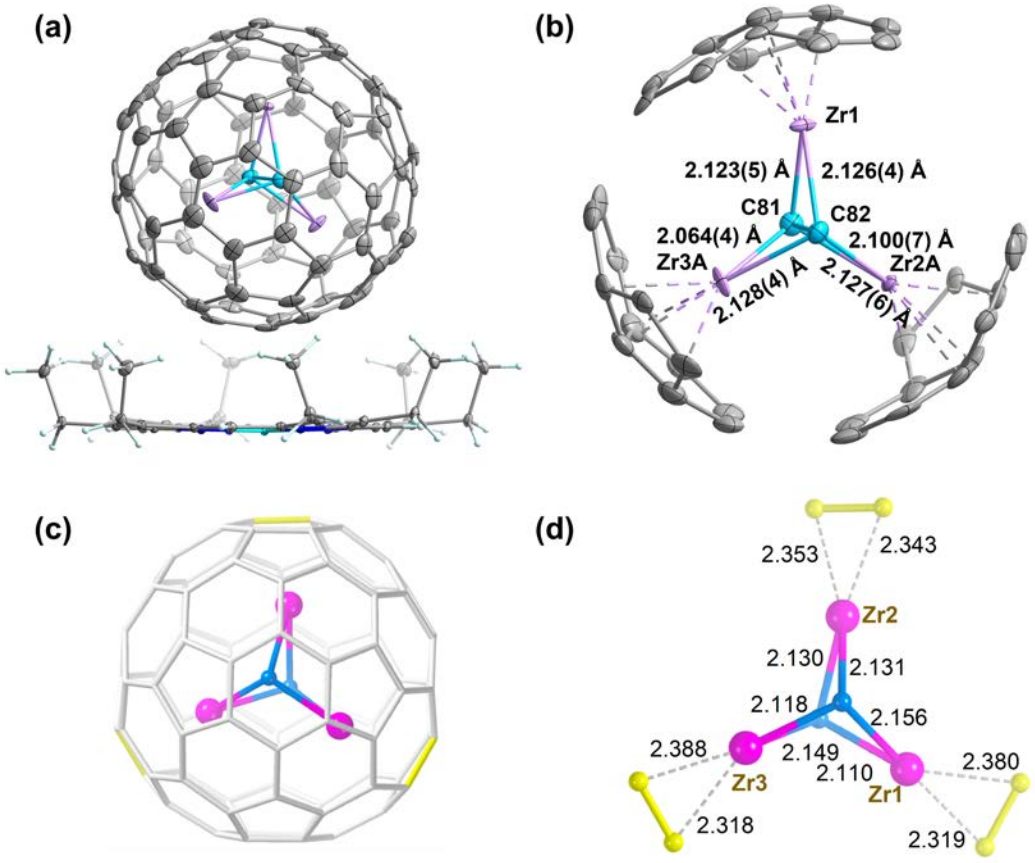


Figure 4. (a) ORTEP drawing of $Zr_3C_2@I_h(7)$-C_{80}·[Ni^{II}OEP] with 20% thermal ellipsoids. Only the major Zr_3C_2 orientation is shown, and the solvent molecules are omitted for clarity. **(b)** Fragment view of the relationship between the Zr_3C_2 cluster and the closest cage portion. The cage C atoms are colored gray, and the encapsulated Zr and C atoms are highlighted as lavender and sky blue, respectively. **(c)** DFT-optimized structure of $Zr_3C_2@I_h(7)$-C_{80}. The nearest bonds of the carbon cage to Zr atoms are highlighted in yellow. **(d)** DFT fragment view of Zr_3C_2 cluster and the closest cage portion. Atomic distances are plotted in Å.

The Zr_3C_2 cluster adopts a slightly distorted trigonal bipyramidal configuration, with each Zr atom coordinating with the C_2 unit. The C_2 unit is oriented at 87.9° relative to the Zr_3 plane, making it nearly perpendicular to the metal framework. This configuration resembles those of $USc_2C_2@D_{5h}(6)$-C_{80} and $CeTi_2C_2@I_h(7)$-C_{80},[49-50] but differs significantly from the batray configurations observed in $Sc_3C_2@I_h(7)$-C_{80} and $Dy_3C_2@I_h(7)$-C_{80}.[51-52] In the Sc_3C_2 and Dy_3C_2 clusters, the C-C bond lengths are 1.29(3) Å and 1.134(22) Å, respectively, indicative of C=C double bond and C≡C triple bond characteristics. In contrast, the C-C bond in the Zr_3C_2 cluster is measured at 1.650(8) Å, which is significantly longer than the typical C≡C triple bond observed in M_2C_2 clusters and also longer than those in Dy_3C_2 and Sc_3C_2 clusters. The unusually long C-C bond length in the Zr_3C_2 cluster suggests a predominantly single-bond character, which was previously reported only in $USc_2C_2@D_{5h}(6)$-C_{80} and $CeTi_2C_2@I_h(7)$-C_{80}.

DFT calculations were employed to validate the configuration of the Zr_3C_2 cluster. A comparative analysis of potential Zr positions indicates that the experimentally determined structure corresponds to the lowest-energy geometry, as shown in Figures 4c-d. The DFT optimized structure supports this long C-C bond length (1.693 Å), in agreement with crystallographic data, and suggests that the C_2 unit exists as a C_2^{6-} anion, analogous to the μ_3-η^2-C_2 unit in β-$ScCrC_2$, where the C-C bond length is approximately 1.60 Å, featuring a C-C single bond character. DFT calculations also suggest that in $Zr_3C_2@I_h(7)$-C_{80}, the interaction between Zr cations and the central μ_3-C_2^{6-} anion is significantly stronger than between the Zr cations and the C_{80} cage. The nearest calculated Zr-$C_{carbide}$ bond length is 2.110 Å, markedly shorter than the nearest Zr-C_{cage} distance (2.318 Å). Notably, this coordination mode observed in the Zr_3C_2 cluster is markedly different from those in conventional zirconium complexes. In most organozirconium systems, mononuclear complexes are more commonly seen than di- or trinuclear species.[53] Furthermore, in the limited examples of trinuclear zirconium complexes, the bridging ligands are usually single nonmetal atoms such as carbon, nitrogen, or oxygen, as exemplified by $[\{Zr(\eta^5\text{-}C_5Me_5)\}_3\{(\mu\text{-}CH)_3SiMe\}(\mu_3\text{-}CSiMe_3)]$,[54] $LZr_3(NHBu\text{-}i)_2(\mu\text{-}NBu\text{-}i)$ (L = $C_5Me_4CH_2CH_2N$),[55] and $Zr_3(NMe_2)_6(\mu\text{-}NMe_2)_3(\mu_3\text{-}O)(\mu_3\text{-}ONMe_2)$.[56] The C_2-bridged Zr_3C_2 cluster stabilized within the fullerene cage adopts a distinct trifoliate-like μ_3-η^2 coordination mode, which is not accessible through conventional ligand frameworks, suggesting the essential role of

the confined carbon cage environment in stabilizing novel metal–carbon bonding patterns.

DFT Studies. DFT calculations were also performed to gain deeper insights into the electronic structures and bonding nature of $Zr_2C_2@C_{2n}$ ($2n$ = 78, 80) and $Zr_3C_2@C_{80}$. The structures were optimized in their singlet spin state using the Kohn-Sham DFT framework with the hybrid PBE0 functional and a triple-zeta basis set.[57-61] For $Zr_2C_2@C_{2n}$, the electronic structure is well described by the formal charge distribution $(Zr_2C_2)^{6+}@(C_{2n})^{6-}$, where each Zr atom donates three electrons to the fullerene cage and one additional electron to the bridged C_2 moiety, leading to a +4 oxidation state. Frontier molecular orbital (MO) analysis reveals that the two highest occupied MOs (HOMOs) are primarily localized on the fullerene cage (Figures 5a-b). In contrast, the lowest unoccupied molecular orbital (LUMO) exhibits significant contributions from the Zr_2C_2 cluster. The LUMO contributions of the Zr_2C_2 cluster for the two EMFs are summarized in Figure S8. For $Zr_2C_2@D_{3h}(5)$-C_{78}, the LUMO is delocalized between the $D_{3h}(5)$-C_{78} cage and the Zr_2C_2 cluster, with major contributions from the 3d orbitals of Zr^{4+} and 2p orbitals of the C_2 moiety, showing an antibonding interaction. The LUMO+1 is primarily localized on the carbon cage, with some contributions from the Zr^{4+} cations. In contrast, for $Zr_2C_2@I_h(7)$-C_{80}, both the LUMO and LUMO+1 are more localized on the Zr_2C_2 cluster, exhibiting stronger MO contributions from the 3d orbitals of Zr^{4+} and 2p orbitals of the C_2 moiety than those seen in $Zr_2C_2@D_{3h}(5)$-C_{78}, suggesting that the electronic structure of Zr_2C_2 cluster is highly dependent on the fullerene cage environment.

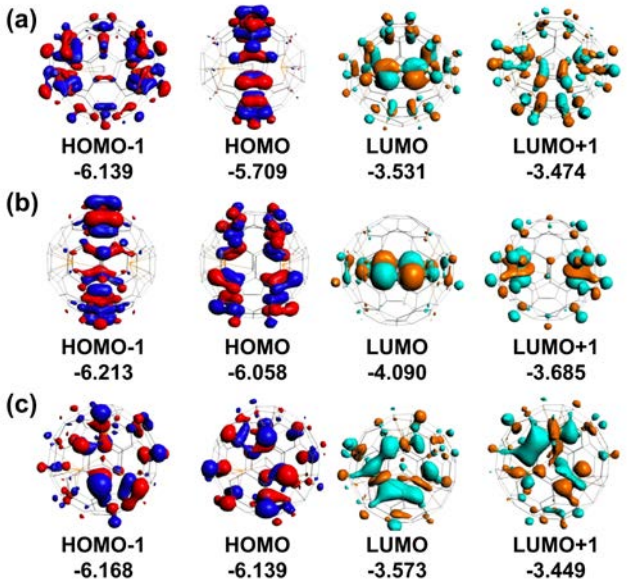


Figure 5. Isosurfaces (±0.03au) of the MOs of (a) $Zr_2C_2@D_{3h}(5)$-C_{78}, (b) $Zr_2C_2@I_h(7)$-C_{80}, and (c) $Zr_3C_2@I_h(7)$-C_{80}. Orbital energies (in eV) are represented below each MO.

For $Zr_3C_2@C_{80}$, the formal electron transfer is assigned as $(Zr_3C_2)^{6+}@(C_{80})^{6-}$, in which the Zr_3C_2 cluster donates six electrons to the fullerene cage (Figure S9). The MO analysis reveals that the HOMO and HOMO-1 are primarily localized on the C_{80} cage, whereas the LUMO and LUMO+1 are largely associated with the Zr_3C_2 cluster (Figures 5c and S10). The carbide unit in Zr_3C_2 cluster can be described as $(C_2)^{6-}$, which is consistent with a single C-C bond, in contrast to the C_2 unit in $Zr_2C_2@C_{2n}$, where it retains a triple-bond character as $(C_2)^{2-}$. This distinction is supported by the computed C-C bond length (1.693 Å in Zr_3C_2 vs. 1.268 Å in Zr_2C_2) in these structures, indicating a significant change in bonding character upon the addition of the third Zr atom.

We have analyzed the chemical bonding within the Zr-carbide clusters, as well as the Zr-cage interaction in the three clusterfullerenes by means of Bader's quantum theory of atoms in molecules (QTAIM).[62] Bader postulated the bond critical point (bcp) between two atoms as a necessary and sufficient condition for the atoms to be bonded. For each of the three Zr-carbide clusters, a bcp is found in between the two C atoms of the carbide. For $Zr_2C_2@D_{3h}(5)$-C_{78}, the density at the bcp (ρ_{bcp}) is 2.68 eÅ^{-3} and the Laplacian of the density ($\nabla^2\rho_{bcp}$) -29.3 eÅ^{-5}, indicating the presence of a very strong covalent bond in line with the triple-bond description from qualitative electron-counting arguments. Similar values are obtained for $Zr_2C_2@I_h(7)$-C_{80} (2.58 eÅ^{-3} and -26.6 eÅ^{-5}). These results are very similar to those found previously for the C_2^{2-} unit in different carbide clusterfullerenes ($Ti_2C_2@C_{78}$, $Y_2C_2@C_{82}$, $Sc_2C_2@C_{2n}$, $Lu_2C_2@C_{2n}$).[63-64] For $Zr_3C_2@I_h(7)$-C_{80}, in contrast, the density at the bcp and the Laplacian of the density are significantly smaller (1.10 eÅ^{-3} and -1.86 eÅ^{-5}) in agreement with the presence of C-C single-bond. Further confirmation of the nature of the C-C bond is provided by natural localized molecular orbitals (NLMO). For Zr_2C_2, there are three NLMO, one σ and two π, that describe the triple bond in the $(C_2)^{2-}$ unit (see Figure 6 for $Zr_2C_2@D_{3h}(5)$-C_{78} and Figure S11 for $Zr_2C_2@I_h(7)$-C_{80}). Conversely, one σ NLMO describes the single C-C bond of the $(C_2)^{6-}$ unit in $Zr_3C_2@I_h(7)$-C_{80} (Figure S12).

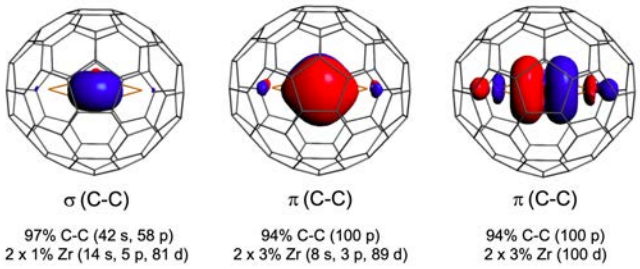


Figure 6. Isosurfaces (±0.03au) of the three NLMO that describe the C-C triple bond of the carbide in $Zr_2C_2@D_{3h}(5)$-C_{78}. Compositions (%) of the carbide unit and the Zr metals are shown.

Delocalization indices, δ(A-B), which provide a quantitative measure of the degree of electron sharing between atoms A and B within QTAIM, have been proposed as a measure of bond order.[65] The values of δ(C-C) in the carbides are 2.38 and 2.26 for $Zr_2C_2@D_{3h}(5)$-C_{78} and $Zr_2C_2@I_h(7)$-C_{80}, respectively, comparable to those found for other M_2C_2 clusterfullerenes.[63] For $Zr_3C_2@I_h(7)$-C_{80}, δ(C-C) is 1.00, in line with the weaker (single) bond in the $(C_2)^{6-}$ unit. Another QTAIM-based index, the localization index (LI), which defines the population of an atomic basin minus the shared electrons, has been proposed recently to measure the oxidation state of electropositive atoms.[66-67] The difference between the LI and atomic number provides a measure of the charge of an atom after the ionic approximation for heteroatomic bonds, which corresponds to the IUPAC definition of oxidation state. Measures of LI(Zr) in the three clusterfullerenes confirm the Zr(IV) oxidation state in all of them. As the two host cages $D_{3h}(5)$-C_{78} and $I_h(7)$-C_{80} are known to be stabilized by formal transfer of six electrons, electron counting

leads to $(C_2)^{2-}$ in Zr_2C_2 and $(C_2)^{6-}$ in Zr_3C_2 clusters. Different population analysis for atomic charges show that the negative charge of the C atoms in the Zr_3C_2 cluster is significantly larger than in the Zr_2C_2 clusters, in line with the formal charge assignment (Table S7).

We find that there is only one Zr-C bcp for each Zr atom within rhombic Zr_2C_2 clusters, which indicates that each metal interacts with the whole C_2 unit, Zr-C_2, as found in Sc_2C_2@C_{84}, Sc_2C_2@C_{82} and Y_2C_2@C_{82}.[63] The parameters at the bcp (Table S8) are similar to those of other metal carbide EMFs ($\nabla^2\rho_{bcp}>0$, $G_{bcp}/\rho_{bcp}\approx1$, $H_{bcp}/\rho_{bcp}<0$) and therefore the bond can be described as covalent with significant degree of charge transfer. For the trifoliate Zr_3C_2 cluster, six Zr-C bcp are found, two for each of the Zr atoms. The parameters at the bcp also point to covalent bonds with strong polarity.

Finally, for the Zr-cage interaction, we find twelve Zr-C bcp in both Zr_2C_2@D_{3h}(5)-C_{78} and Zr_2C_2@I_h(7)-C_{80}, six for each metal atom, which correspond to the C atoms of the nearest cage hexagon (Figure S5). All of them show densities (ρ_{bcp}) within the range 0.45-0.49 eÅ^{-3} and Laplacian values ($\nabla^2\rho_{bcp}$) between 4.6-5.0 eÅ^{-5}, which are comparable to those found for Y_2C_2@C_{82} and Lu_2C_2@C_{2n}.[63-64] The delocalization indices δ(Zr-C) range between 0.28-0.29 for Zr_2C_2@D_{3h}(5)-C_{78} and 0.24-0.29 for Zr_2C_2@I_h(7)-C_{80}, slightly smaller than for Ti_2C_2@C_{78}. The bcp parameters (Table S9) are within the range of other EMFs and, therefore, the Zr-cage interactions are also described as covalent bonds with some degree of charge transfer. The interaction seems to be, however, somewhat less covalent than for Ti_2C_2@C_{78}.[63] On the basis of the M-cage delocalization indices, when comparing to other clusterfullerenes, the interaction between the cage and Zr seems to be somewhat more covalent than for Y or Sc, comparable to Th and less covalent than for U (Table S10).

Spectroscopic Studies. To further explore the spectral properties and electronic structures of these Zr-based carbide clusterfullerenes, UV-vis-NIR absorption spectroscopy was conducted. Figure 7 presents the UV-vis-NIR absorption spectra of the purified Zr-based EMFs alongside images of their solutions in CS_2. The color differences are striking: Zr_2C_2@D_{3h}(5)-C_{78} appears indigo, whereas both Zr_2C_2@I_h(7)-C_{80} and Zr_3C_2@I_h(7)-C_{80} appear golden. Zr_2C_2@D_{3h}(5)-C_{78} exhibits characteristic absorption peaks at 517 and 587 nm, accompanied by a shoulder peak at 671 nm. In contrast, the spectra of Zr_2C_2@I_h(7)-C_{80} and Zr_3C_2@I_h(7)-C_{80} are relatively featureless, exhibiting no prominent absorption features. Notably, although the absorption profile of Zr_2C_2@D_{3h}(5)-C_{78} shows similar peak positions to those of Ti_2C_2@D_{3h}(5)-C_{78},[14] Ti_2S@D_{3h}(5)-C_{78},[68] and Sc_3N@D_{3h}(5)-C_{78},[69] it exhibits distinct differences in peak intensities and overall spectral profile, likely due to the variations in the degree of orbital overlap between the D_{3h}(5)-C_{78} π-system and Zr_2C_2 or these clusters. In contrast, the spectra of Zr_2C_2@I_h(7)-C_{80} and Zr_3C_2@I_h(7)-C_{80} align well with those of EMFs based on $(I_h(7)\text{-}C_{80})^{6-}$, such as $(Sc_3N)^{6+}$@$(C_{80})^{6-}$ and $(U_2C_2)^{6+}$@$(C_{80})^{6-}$,[47, 70] indicating that the electronic structure of Zr_2C_2@I_h(7)-C_{80} and Zr_3C_2@I_h(7)-C_{80} can be described as $(Zr_2C_2)^{6+}$@$(I_h(7)\text{-}C_{80})^{6-}$ and $(Zr_3C_2)^{6+}$@$(I_h(7)\text{-}C_{80})^{6-}$, in excellent agreement with the theoretical calculation results.

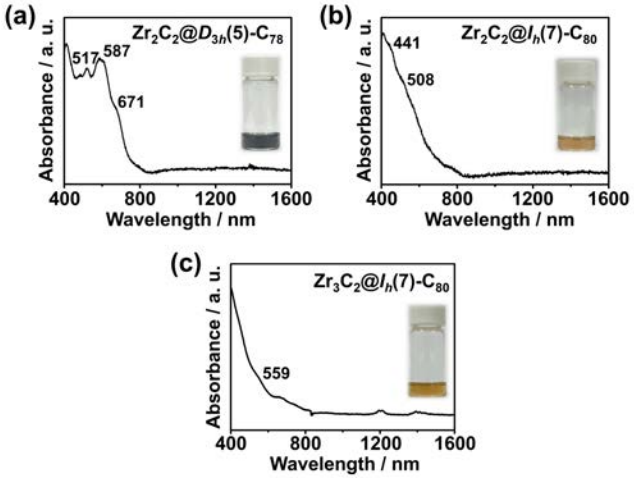


Figure 7. UV-vis-NIR spectra of purified (a) Zr_2C_2@D_{3h}(5)-C_{78}, (b) Zr_2C_2@I_h(7)-C_{80}, and (c) Zr_3C_2@I_h(7)-C_{80}. The inserts show the photographs of corresponding samples dissolved in CS_2 solution.

CONCLUSIONS

In summary, we report the first encapsulation of Zr-based carbide clusters within fullerene cages, overcoming a synthetic challenge that has persisted for over three decades. By utilizing an optimized synthesis strategy with zirconium carbide as the metal source, we obtained three Zr-based carbide clusterfullerenes, namely Zr_2C_2@D_{3h}(5)-C_{78}, Zr_2C_2@I_h(7)-C_{80}, and Zr_3C_2@I_h(7)-C_{80}. Detailed structural analyses revealed that the Zr_2C_2 clusters form planar rhombic configurations, revealing the influence of metal ionic size on cluster geometry. The Zr_3C_2 cluster adopts a trifoliate configuration with a μ_3-η^2 coordination mode, which differs significantly from those observed in conventional organozirconium complexes, suggesting the essential role of the confined chemical environment of carbon cages in stabilizing unprecedented metal-carbon bonding patterns. Notably, the Zr_2C_2 clusters contain a triple-bonded C≡C unit, while the Zr_3C_2 cluster features a single-bonded C-C bridge. Combined experimental and theoretical studies further reveal the electronic structures of the Zr-based EMFs as $(Zr_2C_2)^{6+}$@$(C_{2n})^{6-}$ ($2n$ = 78, 80) and $(Zr_3C_2)^{6+}$@$(I_h(7)\text{-}C_{80})^{6-}$. This work not only offers structural understanding into three novel Zr-based carbide clusterfullerenes but also provides new insights into the mechanisms of arc-discharge reaction and the formation of EMFs. Furthermore, this work also provides a substantial guideline for the encapsulation of new elements into fullerene cages, establishing a foundation for the design and synthesis of novel EMFs.

EXPERIMENTAL DETAILS

Spectroscopic Studies. Positive-ion mode matrix-assisted laser desorption ionization time-of-flight (MALDI-TOF) mass spectrometry (Bruker, Germany) was utilized for mass characterization. The UV-vis-NIR spectra of purified samples in CS_2 solution were obtained using a Cary 5000 UV-vis-NIR spectrophotometer (Agilent, USA).

X-ray Crystallographic Study. The black block crystals of Zr_2C_2@D_{3h}(5)-C_{78}, Zr_2C_2@I_h(7)-C_{80} and Zr_3C_2@I_h(7)-C_{80} were obtained through slow diffusion of the CS_2 solution containing the respective metallofullerene compounds into a benzene solution of [Ni^{II}(OEP)]. Single-crystal X-ray data for samples were collected using a diffractometer (Bruker D8 Venture) equipped with a CCD detector. Absorption correction was carried out using the multiscan

method. The structures were determined via direct methods and refined on F^2 using full-matrix least-squares refinement with the SHELXL2015 crystallographic software.[71-72] Hydrogen atoms were placed at calculated positions and constrained with isotropic thermal parameters. Crystallographic data for $Zr_2C_2@D_{3h}(5)$-C_{78}, $Zr_2C_2@I_h(7)$-C_{80}, and $Zr_3C_2@I_h(7)$-C_{80} are presented in Table S1.

Computational Details. The Amsterdam Density Functional (ADF, v. 2019) package was used to perform the Kohn-Sham density functional theory (DFT) calculations.[57] The hybrid PBE0 exchange correlation functional was employed in conjunction with all-electron triple-ζ polarized (TZP) Slater-type orbital (STO) basis sets quality.[58-61] Relativistic effects were included by means of the scalar relativistic (SR) zero-order regular approximation (ZORA). D3 dispersion corrections by Grimme were considered in the calculations.[73-75]

ASSOCIATED CONTENT

Supporting Information.

HPLC profiles for the separation of $Zr_2C_2@D_{3h}(5)$-C_{78}, $Zr_2C_2@I_h(7)$-C_{80}, and $Zr_3C_2@I_h(7)$-C_{80}; additional single-crystal structural parameters of the three EMFs; and complementary results from computation studies. This material is available free of charge via the Internet at http://pubs.acs.org.

Accession Codes

CCDC 2388915, 2388916, and 2474514 contain the supplementary crystallographic data for this paper. These data can be obtained free of charge via www.ccdc.cam.ac.uk/data_request/cif, or by emailing data_request@ccdc.cam.ac.uk, or by contacting The Cambridge Crystallographic Data Centre, 12 Union Road, Cambridge CB2 1EZ, UK; fax: +44 1223 336033.

AUTHOR INFORMATION

Corresponding Authors

*E-mail: chenning@suda.edu.cn
*E-mail: antonio.rodriguezf@urv.cat
*E-mail: yryao@suda.edu.cn

Author Contributions

†Yi Shen and Laura Abella contributed equally to this work.

Notes

The authors declare no competing financial interests.

ACKNOWLEDGMENT

N. C. thanks the National Natural Science Foundation of China (NSFC No. 52172051), the Natural Science Foundation of Jiangsu Province (BK20200041), and the Priority Academic Program Development of Jiangsu Higher Education Institutions (PAPD). Y.-R. Y. thanks the National Science Foundation of China (22301288) and the Anhui Provincial Natural Science Foundation (2308085MB31). A.R.-F. and J.M.P. thank the Spanish Ministry of Science, Innovation and Universities (grant PID2023-149905NB-I00 funded by MICIU/AEI/10.13039/501100011033 by "ERDF/EU"), the Generalitat de Catalunya (grant 2021 SGR 00110) and the URV for support.

REFERENCES

(1) Popov, A. A.; Yang, S.; Dunsch, L. Endohedral Fullerenes. *Chem. Rev.* **2013,** *113* (8), 5989-6113.

(2) Yang, S.; Wei, T.; Jin, F. When metal clusters meet carbon cages: endohedral clusterfullerenes. *Chem. Soc. Rev.* **2017,** *46* (16), 5005-5058.

(3) Lu, X.; Akasaka, T.; Slanina, Z. Handbook of fullerene science and technology. *Springer, Singapore,* **2022**; pp 1-1035.

(4) Zhang, K.; Wang, C.; Zhang, M.; Bai, Z.; Xie, F.-F.; Tan, Y.-Z.; Guo, Y.; Hu, K.-J.; Cao, L.; Zhang, S.; Tu, X.; Pan, D.; Kang, L.; Chen, J.; Wu, P.; Wang, X.; Wang, J.; Liu, J.; Song, Y.; Wang, G.; Song, F.; Ji, W.; Xie, S.-Y.; Shi, S.-F.; Reed, M. A.; Wang, B. A Gd@C_{82} single-molecule electret. *Nat. Nanotechnol.* **2020,** *15* (12), 1019-1024.

(5) Qiu, J.; Abella, L.; Du, X.; Cao, Z.; He, Z.; Meng, Q.; Yan, Y.; Poblet, J. M.; Sun, L.; Rodríguez-Fortea, A.; Chen, N. CaY@C_{2n}: Exploring Molecular Qubits with Ca–Y Metal–Metal Bonds. *J. Am. Chem. Soc.* **2024,** *146* (35), 24310-24319.

(6) Liang, X.-J.; Shen, D.-W.; Garfield, S.; Gottesman, M. M. Mislocalization of membrane proteins associated with multidrug resistance in cisplatin-resistant cancer cell lines. *Cancer Res.* **2003,** *63* (18), 5909-5916.

(7) Wu, B.; Wang, T.; Feng, Y.; Zhang, Z.; Jiang, L.; Wang, C. Molecular magnetic switch for a metallofullerene. *Nat. Commun.* **2015,** *6* (1), 6468.

(8) Hu, Z.; Dong, B.-W.; Liu, Z.; Liu, J.-J.; Su, J.; Yu, C.; Xiong, J.; Shi, D.-E.; Wang, Y.; Wang, B.-W.; Ardavan, A.; Shi, Z.; Jiang, S.-D.; Gao, S. Endohedral Metallofullerene as Molecular High Spin Qubit: Diverse Rabi Cycles in $Gd_2@C_{79}N$. *J. Am. Chem. Soc.* **2018,** *140* (3), 1123-1130.

(9) Liu, F.; Velkos, G.; Krylov, D. S.; Spree, L.; Zalibera, M.; Ray, R.; Samoylova, N. A.; Chen, C.-H.; Rosenkranz, M.; Schiemenz, S.; Ziegs, F.; Nenkov, K.; Kostanyan, A.; Greber, T.; Wolter, A. U. B.; Richter, M.; Büchner, B.; Avdoshenko, S. M.; Popov, A. A. Air-stable redox-active nanomagnets with lanthanide spins radical-bridged by a metal–metal bond. *Nat. Commun.* **2019,** *10* (1), 571.

(10) Lin, Y.; Lin, Z.; Lv, S.; Shui, Y.; Zhu, W.; Zhang, Z.; Yang, W.; Zhao, J.; Gu, H.; Xia, J.; Wang, D.; Du, F.; Zhu, A.; Liu, J.; Cai, H.; Wang, B.; Zhang, N.; Wang, H.; Liu, X.; Liu, T.; Kong, C.; Zhou, D.; Chen, S.; Yang, Z.; Li, T.; Ma, W.; Fang, G.; Echegoyen, L.; Xing, G.; Yang, S.; Yang, T.; Cai, W.; Li, M.; Huang, W.; Liang, C. A Nd@C_{82}–polymer interface for efficient and stable perovskite solar cells. *Nature* **2025,** *642* (8066), 78-84.

(11) Stevenson, S.; Rice, G.; Glass, T.; Harich, K.; Cromer, F.; Jordan, M. R.; Craft, J.; Hadju, E.; Bible, R.; Olmstead, M. M.; Maitra, K.; Fisher, A. J.; Balch, A. L.; Dorn, H. C. Small-bandgap endohedral metallofullerenes in high yield and purity. *Nature* **1999,** *401* (6748), 55-57.

(12) Wei, T.; Wang, S.; Lu, X.; Tan, Y.; Huang, J.; Liu, F.; Li, Q.; Xie, S.; Yang, S. Entrapping a Group-VB Transition Metal, Vanadium, within an Endohedral Metallofullerene: $V_xSc_{3-x}N@I_h$-C_{80} (x = 1, 2). *J. Am. Chem. Soc.* **2016,** *138* (1), 207-214.

(13) Yu, P.; Shen, W.; Bao, L.; Pan, C.; Slanina, Z.; Lu, X. Trapping an unprecedented Ti_3C_3 unit inside the icosahedral C_{80} fullerene: a crystallographic survey. *Chem. Sci.* **2019,** *10* (47), 10925-10930.

(14) Yu, P.; Bao, L.; Yang, L.; Hao, D.; Jin, P.; Shen, W.; Fang, H.; Akasaka, T.; Lu, X. Crystallographic Characterization of $Ti_2C_2@D_{3h}(5)$-C_{78}, $Ti_2C_2@C_{3v}(8)$-C_{82}, and $Ti_2C_2@C_s(6)$-C_{82}: Identification of Unsupported Ti_2C_2 Cluster with Cage-Dependent Configurations. *Inorg. Chem.* **2020,** *59* (13), 9416-9423.

(15) Guo, B. C.; Wei, S.; Purnell, J.; Buzza, S.; Castleman, A. W. Metallo-Carbohedrenes [$M_8C_{12}^+$ (M = V, Zr, Hf, and Ti)]: A Class of Stable Molecular Cluster Ions. *Science* **1992,** *256* (5056), 515-516.

(16) Li, S.; Wu, H.; Wang, L.-S. Probing the Electronic Structure of Metallocarbohedrenes: M_8C_{12} (M = Ti, V, Cr, Zr, Nb). *J. Am. Chem. Soc.* **1997,** *119* (32), 7417-7422.

(17) Driscoll, N.; Richardson, A. G.; Maleski, K.; Anasori, B.; Adewole, O.; Lelyukh, P.; Escobedo, L.; Cullen, D. K.; Lucas, T. H.; Gogotsi, Y.; Vitale, F. Two-Dimensional Ti_3C_2 MXene for High-Resolution Neural Interfaces. *ACS Nano* **2018,** *12* (10), 10419-10429.

(18) Fu, Z.; Hai, G.; Ma, X.-X.; Legut, D.; Zheng, Y.; Chen, X. Rational design of MXene-based vacancy-confined single-atom catalyst for efficient oxygen evolution reaction. *J. Energy Chem.* **2024,** *98*, 663-669.

(19) Wei, S.; Guo, B. C.; Purnell, J.; Buzza, S.; Castleman, A. W. Metallo-Carbohedrenes: Formation of Multicage Structures. *Science* **1992,** *256* (5058), 818-820.

(20) Chuai, P.; Hu, Z.; Yao, Y.-R.; Jiang, Z.; Ullah, A.; Zhao, Y.; Cheng, W.; Chen, M.; Coronado, E.; Yang, S.; Shi, Z. Lanthanide–nickel molecular intermetallic complexes featuring a ligand-free Ni^{2-} anion in endohedral fullerenes. *Nat. Chem.* **2025,** *17* (7), 1053-1057.

(21) Junghans, K.; Schlesier, C.; Kostanyan, A.; Samoylova, N. A.; Deng, Q.; Rosenkranz, M.; Schiemenz, S.; Westerström, R.; Greber, T.; Büchner, B.; Popov, A. A. Methane as a Selectivity Booster in the Arc-Discharge Synthesis of Endohedral Fullerenes: Selective Synthesis of the Single-Molecule Magnet $Dy_2TiC@C_{80}$ and Its Congener $Dy_2TiC_2@C_{80}$. *Angew. Chem. Int. Ed.* **2015,** *54* (45), 13411-13415.

(22) Guan, R.; Huang, J.; Xin, J.; Chen, M.; Du, P.; Li, Q.; Tan, Y.-Z.; Yang, S.; Xie, S.-Y. A stabilization rule for metal carbido cluster bearing μ^3-carbido single-atom-ligand encapsulated in carbon cage. *Nat. Commun.* **2024,** *15* (1), 150.

(23) Wei, T.; Jin, F.; Guan, R.; Huang, J.; Chen, M.; Li, Q.; Yang, S. Blending Non-Group-3 Transition Metal and Rare-Earth Metal into a C_{80} Fullerene Cage with D_{5h} Symmetry. *Angew. Chem. Int. Ed.* **2018,** *57* (32), 10273-10277.

(24) Akiyama, K.; Sueki, K.; Kodama, T.; Kikuchi, K.; Takigawa, Y.; Nakahara, H.; Ikemoto, I.; Katada, M. New fullerenes of a group IV element: Hf metallofullerenes. *Chem. Phys. Lett.* **2000,** *317* (3), 490-496.

(25) Cong, H.; Yu, B.; Akasaka, T.; Lu, X. Endohedral metallofullerenes: An unconventional core–shell coordination union. *Coord. Chem. Rev.* **2013,** *257* (21), 2880-2898.

(26) Guo, T.; Diener, M. D.; Chai, Y.; Alford, M. J.; Haufler, R. E.; McClure, S. M.; Ohno, T.; Weaver, J. H.; Scuseria, G. E.; Smalley, R. E. Uranium Stabilization of C_{28}: A Tetravalent Fullerene. *Science* **1992,** *257* (5077), 1661-1664.

(27) Dunk, P. W.; Kaiser, N. K.; Mulet-Gas, M.; Rodríguez-Fortea, A.; Poblet, J. M.; Shinohara, H.; Hendrickson, C. L.; Marshall, A. G.; Kroto, H. W. The Smallest Stable Fullerene, $M@C_{28}$ (M = Ti, Zr, U): Stabilization and Growth from Carbon Vapor. *J. Am. Chem. Soc.* **2012,** *134* (22), 9380-9389.

(28) Muñoz-Castro, A.; King, R. B. Formation of Spherical Aromatic Endohedral Metallic Fullerenes. Evaluation of Magnetic Properties of $M@C_{28}$ (M = Ti, Zr, and Hf) from DFT calculations. *Inorg. Chem.* **2017,** *56* (24), 15251-15258.

(29) Saha, S. K.; Chowdhury, D. P.; Das, S. K.; Guin, R. Encapsulation of radioactive isotopes into C_{60} fullerene cage by recoil implantation technique. *Nucl. Instrum. Meth. B* **2006,** *243* (2), 277-281.

(30) Bandow, S.; Shinohara, H.; Saito, Y.; Ohkohchi, M.; Ando, Y. High yield synthesis of lanthanofullerenes via lanthanum carbide. *J. Phys. Chem.* **1993**, *97* (23), 6101-6103.

(31) Bandow, S.; Saito, Y. Encapsulation of ZrC and V_4C_3 in graphite nanoballs via arc burning of metal carbides/graphite composites. *Jpn. J. Appl. Phys.* **1993,** *32* (11B), L1677.

(32) Merchant, P.; Veillon, C. Characterization of a d.c. arc plasma jet in argon as an atomization and excitation source for atomic spectroscopy. *Anal. Chim. Acta* **1974,** *70* (1), 17-24.

(33) Cai, W.; Alvarado, J.; Metta-Magaña, A.; Chen, N.; Echegoyen, L. Interconversions between Uranium Mono-metallofullerenes: Mechanistic Implications and Role of Asymmetric Cages. *J. Am. Chem. Soc.* **2020,** *142* (30), 13112-13119.

(34) Yang, H.; Jin, H.; Wang, X.; Liu, Z.; Yu, M.; Zhao, F.; Mercado, B. Q.; Olmstead, M. M.; Balch, A. L. X-ray Crystallographic Characterization of New Soluble Endohedral Fullerenes Utilizing the Popular C_{82} Bucky Cage. Isolation and Structural Characterization of $Sm@C_{3v}(7)$-C_{82}, $Sm@C_s(6)$-C_{82}, and $Sm@C_2(5)$-C_{82}. *J. Am. Chem. Soc.* **2012,** *134* (34), 14127-14136.

(35) Maeda, Y.; Matsunaga, Y.; Wakahara, T.; Takahashi, S.; Tsuchiya, T.; Ishitsuka, M. O.; Hasegawa, T.; Akasaka, T.; Liu, M. T. H.; Kokura, K.; Horn, E.; Yoza, K.; Kato, T.; Okubo, S.; Kobayashi, K.; Nagase, S.; Yamamoto, K. Isolation and Characterization of a Carbene Derivative of $La@C_{82}$. *J. Am. Chem. Soc.* **2004,** *126* (22), 6858-6859.

(36) Wang, Y.; Morales-Martínez, R.; Zhang, X.; Yang, W.; Wang, Y.; Rodríguez-Fortea, A.; Poblet, J. M.; Feng, L.; Wang, S.; Chen, N. Unique Four-Electron Metal-to-Cage Charge Transfer of Th to a C_{82} Fullerene Cage: Complete Structural Characterization of $Th@C_{3v}(8)$-C_{82}. *J. Am. Chem. Soc.* **2017,** *139* (14), 5110-5116.

(37) Chen, C.-H.; Krylov, D. S.; Avdoshenko, Stanislav M.; Liu, F.; Spree, L.; Yadav, R.; Alvertis, A.; Hozoi, L.; Nenkov, K.; Kostanyan, A.; Greber, T.; Wolter, A. U. B.; Popov, A. A. Selective arc-discharge synthesis of Dy_2S-clusterfullerenes and their isomer-dependent single molecule magnetism. *Chem. Sci.* **2017**, *8* (9), 6451-6465.

(38) Dunk, P. W.; Kaiser, N. K.; Hendrickson, C. L.; Quinn, J. P.; Ewels, C. P.; Nakanishi, Y.; Sasaki, Y.; Shinohara, H.; Marshall, A. G.; Kroto, H. W. Closed network growth of fullerenes. *Nat. Commun.* **2012,** *3* (1), 855.

(39) von Helden, G.; Gotts, N. G.; Bowers, M. T. Experimental evidence for the formation of fullerenes by collisional heating of carbon rings in the gas phase. *Nature* **1993,** *363* (6424), 60-63.

(40) Dunk, P. W.; Mulet-Gas, M.; Nakanishi, Y.; Kaiser, N. K.; Rodríguez-Fortea, A.; Shinohara, H.; Poblet, J. M.; Marshall, A. G.; Kroto, H. W. Bottom-up formation of endohedral mono-metallofullerenes is directed by charge transfer. *Nat. Commun.* **2014,** *5* (1), 5844.

(41) Ugarte, D. Curling and closure of graphitic networks under electron-beam irradiation. *Nature* **1992,** *359* (6397), 707-709.

(42) Chuvilin, A.; Kaiser, U.; Bichoutskaia, E.; Besley, N. A.; Khlobystov, A. N. Direct transformation of graphene to fullerene. *Nat. Chem.* **2010,** *2* (6), 450-453.

(43) Kurihara, H.; Lu, X.; Iiduka, Y.; Nikawa, H.; Hachiya, M.; Mizorogi, N.; Slanina, Z.; Tsuchiya, T.; Nagase, S.; Akasaka, T. X-ray Structures of $Sc_2C_2@C_{2n}$ (n = 40–42): In-Depth Understanding of the Core–Shell Interplay in Carbide Cluster Metallofullerenes. *Inorg. Chem.* **2012,** *51* (1), 746-750.

(44) Yang, W.; Velkos, G.; Sudarkova, S.; Büchner, B.; Avdoshenko, S. M.; Liu, F.; Popov, A. A.; Chen, N. Carbon cage isomers and magnetic Dy···Dy interactions in $Dy_2O@C_{88}$ and $Dy_2C_2@C_{88}$ metallofullerenes. *Inorg. Chem. Front.* **2022**, *9* (22), 5805-5819.

(45) Zhang, J.; Bowles, F. L.; Bearden, D. W.; Ray, W. K.; Fuhrer, T.; Ye, Y.; Dixon, C.; Harich, K.; Helm, R. F.; Olmstead, M. M.; Balch, A. L.; Dorn, H. C. A missing link in the transformation from asymmetric to symmetric metallofullerene cages implies a top-down fullerene formation mechanism. *Nat. Chem.* **2013,** *5* (10), 880-885.

(46) Sado, Y.; Aoyagi, S.; Izumi, N.; Kitaura, R.; Kowalczyk, T.; Wang, J.; Irle, S.; Nishibori, E.; Sugimoto, K.; Shinohara, H. Structure of Tm_2 and Tm_2C_2 encapsulated in low-symmetry $C_{82}(C_s(6))$ fullerene cage by single crystal X-ray diffraction. *Chem. Phys. Lett.* **2014,** *600*, 38-42.

(47) Zhuang, J.; Abella, L.; Sergentu, D.-C.; Yao, Y.-R.; Jin, M.; Yang, W.; Zhang, X.; Li, X.; Zhang, D.; Zhao, Y.; Li, X.; Wang, S.; Echegoyen, L.; Autschbach, J.; Chen, N. Diuranium(IV) Carbide Cluster U_2C_2 Stabilized Inside Fullerene Cages. *J. Am. Chem. Soc.* **2019,** *141* (51), 20249-20260.

(48) Chen, C.-H.; Abella, L.; Cerón, M. R.; Guerrero-Ayala, M. A.; Rodríguez-Fortea, A.; Olmstead, M. M.; Powers, X. B.; Balch, A. L.; Poblet, J. M.; Echegoyen, L. Zigzag Sc_2C_2 Carbide Cluster inside a [88]Fullerene Cage with One Heptagon, $Sc_2C_2@C_s$(hept)-C_{88}: A Kinetically Trapped Fullerene Formed by C_2 Insertion? *J. Am. Chem. Soc.* **2016,** *138* (39), 13030-13037.

(49) Jiang, H.; Yu, X.; Guo, M.; Yao, Y.-R.; Meng, Q.; Echegoyen, L.; Autschbach, J.; Chen, N. USc_2C_2 and USc_2NC Clusters with U–C Triple Bond Character Stabilized Inside Fullerene Cages. *J. Am. Chem. Soc.* **2023,** *145* (10), 5645-5654.

(50) Jiang, Z.; Hu, Z.; Yao, Y.-R.; Han, X.; Xin, J.; Yang, S. Diatomic C_2/NC Ligand Induced Conformation Variation of Trimetallic Clusters within a Carbon Cage. *J. Am. Chem. Soc.* **2025,** *147* (10), 8939-8947.

(51) Fang, H.; Cong, H.; Suzuki, M.; Bao, L.; Yu, B.; Xie, Y.; Mizorogi, N.; Olmstead, M. M.; Balch, A. L.; Nagase, S.; Akasaka, T.; Lu, X. Regioselective Benzyl Radical Addition to an Open-Shell Cluster Metallofullerene. Crystallographic Studies of Cocrystallized $Sc_3C_2@I_h$-C_{80} and Its Singly Bonded Derivative. *J. Am. Chem. Soc.* **2014,** *136* (29), 10534-10540.

(52) Jin, F.; Xin, J.; Guan, R.; Xie, X.-M.; Chen, M.; Zhang, Q.; Popov, A. A.; Xie, S.-Y.; Yang, S. Stabilizing a three-center single-electron metal–metal bond in a fullerene cage. *Chem. Sci.* **2021,** *12* (20), 6890-6895.

(53) Cibuzar, M. P.; Novas, B. T.; Waterman, R. Zirconium Complexes. In *Comprehensive Coordination Chemistry III*, Constable, E. C.; Parkin, G.; Que Jr, L., Eds. Elsevier: Oxford, **2021**; pp 162-196.

(54) Greño, M.; Horno, E. d.; Mena, M.; Pérez-Redondo, A.; Varela-Izquierdo, V.; Yélamos, C. Group 4 Half-Sandwich Tris(trimethylsilylmethyl) Complexes: Thermal Decomposition and Reactivity with N,N-Dimethylamine–Borane. *Inorg. Chem.* **2017,** *56* (18), 11220-11229.

(55) Oishi, M.; Nakanishi, Y.; Suzuki, H. Selective Incorporation of Primary Amines into a Trizirconium Imido System and Catalyic Cyclization of Aminoalkynes. *Inorg. Chem.* **2017,** *56* (16), 9802-9813.

(56) Boutonnet, F.; Zablocka, M.; Igau, A.; Jaud, J.; Majoral, J.-P.; Schamberger, J.; Erker, G.; Werner, S.; Krüger, C. Syntheses and crystallographic characterizations of trinuclear (μ_3-O) zirconium complexes. *J. Chem. Soc., Chem. Commun.* **1995,** (8), 823-824.

(57) te Velde, G.; Bickelhaupt, F. M.; Baerends, E. J.; Fonseca Guerra, C.; van Gisbergen, S. J. A.; Snijders, J. G.; Ziegler, T. Chemistry with ADF. *J. Comput. Chem.* **2001,** *22* (9), 931-967.

(58) Perdew, J. P.; Burke, K.; Ernzerhof, M. Generalized Gradient Approximation Made Simple. *Phys. Rev. Lett.* **1996,** *77* (18), 3865-3868.

(59) Adamo, C.; Barone, V. Toward reliable density functional methods without adjustable parameters: The PBE0 model. *J. Chem. Phys.* **1999,** *110* (13), 6158-6170.

(60) Perdew, J. P. Density-functional approximation for the correlation energy of the inhomogeneous electron gas. *Phys. Rev. B* **1986,** *33* (12), 8822-8824.

(61) Becke, A. D. Density functional calculations of molecular bond energies. *J. Chem. Phys.* **1986,** *84* (8), 4524-4529.

(62) Richard, F.; Bader, R. Atoms in molecules: a quantum theory. *Oxford University Press, Oxford* **1990**.

(63) Popov , A. A.; Dunsch, L. Bonding in Endohedral Metallofullerenes as Studied by Quantum Theory of Atoms in Molecules. *Chem. Eur. J.* **2009,** *15* (38), 9707-9729.

(64) Shen, W.; Bao, L.; Yu, P.; Yang, L.; Li, B.; Yu, P.; Jin, P.; Lu, X. Isolation and crystallographic characterization of $Lu_2C_2@C_{2n}$ ($2n$ = 88–92): Internal cluster stretching upon outer cage expansion. *Carbon* **2020,** *164*, 157-163.

(65) Outeiral, C.; Vincent, M. A.; Martín Pendás, Á.; Popelier, P. L. A. Revitalizing the concept of bond order through delocalization measures in real space. *Chem. Sci.* **2018,** *9* (25), 5517-5529.

(66) Day, C. S.; Do, C. D.; Odena, C.; Benet-Buchholz, J.; Xu, L.; Foroutan-Nejad, C.; Hopmann, K. H.; Martin, R. Room-Temperature-Stable Magnesium Electride via Ni(II) Reduction. *J. Am. Chem. Soc.* **2022,** *144* (29), 13109-13117.

(67) Mehara, J.; Koovakattil Surendran, A.; van Wieringen, T.; Setia, D.; Foroutan-Nejad, C.; Straka, M.; Rulíšek, L.; Roithová, J. Cationic Gold(II) Complexes: Experimental and Theoretical Study. *Chem. Eur. J.* **2022,** *28* (60), e202201794.

(68) Li, F.-F.; Chen, N.; Mulet-Gas, M.; Triana, V.; Murillo, J.; Rodríguez-Fortea, A.; Poblet, J. M.; Echegoyen, L. $Ti_2S@D_{3h}$(24109)-C_{78}: a sulfide cluster metallofullerene containing only transition metals inside the cage. *Chem. Sci.* **2013,** *4* (9), 3404-3410.

(69) Olmstead, M. M.; de Bettencourt-Dias, A.; Duchamp, J. C.; Stevenson, S.; Marciu, D.; Dorn, H. C.; Balch, A. L. Isolation and Structural Characterization of the Endohedral Fullerene $Sc_3N@C_{78}$. *Angew. Chem. Int. Ed.* **2001,** *40* (7), 1223-1225.

(70) Feng, Y.; Hu, Y.; Luo, T.; Yuan, C.; Zhu, W.; Gao, M.; Huo, X. Regulating the electronic and spin structure of endohedral metallofullerenes: a case investigation of $Sc_3N@C_{80}$ and $Sc_3C_2@C_{80}$. *Dalton Trans.* **2022,** *51* (48), 18734-18740.

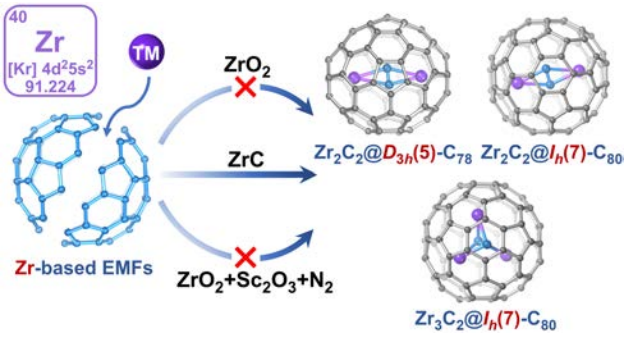
(71) Dolomanov, O. V.; Bourhis, L. J.; Gildea, R. J.; Howard, J. A. K.; Puschmann, H. OLEX2: a complete structure solution, refinement and analysis program. *J. Appl. Crystallogr.* **2009,** *42* (2), 339-341.

(72) Sheldrick, G. Crystal structure refinement with SHELXL. *Acta Crystallogr. C* **2015,** *71* (1), 3-8.

(73) Lenthe, E. v.; Baerends, E. J.; Snijders, J. G. Relativistic regular two-component Hamiltonians. *J. Chem. Phys.* **1993,** *99* (6), 4597-4610.

(74) Grimme, S.; Antony, J.; Ehrlich, S.; Krieg, H. A consistent and accurate ab initio parametrization of density functional dispersion correction (DFT-D) for the 94 elements H-Pu. *J. Chem. Phys.* **2010,** *132* (15), 154104.

(75) Grimme, S.; Ehrlich, S.; Goerigk, L. Effect of the damping function in dispersion corrected density functional theory. *J. Comput. Chem.* **2011,** *32* (7), 1456-1465.


40
Zr
[Kr] 4d²5s²
91.224
TM
Zr-based EMFs
ZrO2
ZrC
ZrO2+Sc2O3+N2
Zr2C2@D3h(5)-C78
Zr2C2@Ih(7)-C80
Zr3C2@Ih(7)-C80